Nano-Micro Letters

e-ISSN 2150-5551
CN 31-2103/TB

ARTICLE

https://doi.org/10.1007/s40820-026-02210-y

Cite as
Nano-Micro Lett.
(2026) 18:364

Received: 5 January 2026
Accepted: 8 April 2026

Electronic Delocalization of Fe Atom–Cluster for Long-Term Stable Electromagnetic Wave Absorption in Marine Environments

Shaocong Zhong[1], Xinyu Wang[1], Rurong Zou[1,2], Chang Long[2], Pianpian Zhang[1] ✉, Xueting Zhang[1], Zihao Zhao[1], Ying Liu[1], Can Cui[1], Yanan Yang[1] ✉, Long Xia[1] ✉

HIGHLIGHTS

- Fe cluster–single-atom synergy induces electron delocalization and charge redistribution, enabling multicenter coupling for enhanced electromagnetic wave attenuation.
- The synergistic electronic regulation significantly strengthens dielectric loss and conduction loss, leading to high-efficiency electromagnetic wave absorption at low filler loadings.
- Fe clusters preferentially adsorb Cl^-, generating localized negatively charged regions that mitigate ionic attack on single-atom sites and improve durability in marine conditions.

ABSTRACT High-performance electromagnetic wave (EMW) absorbers with environmental adaptability are essential for advanced maritime stealth and electromagnetic protection. Herein, we design a synergistic absorber integrating Fe clusters (Fe_{AC}) and single atoms (Fe_{SA}) to tackle the issue of EMW attenuation under high-salinity and humidity marine conditions. First-principles calculations and experiments reveal that Fe_{AC} and Fe_{SA} anchored on a π-conjugated carbon support form a delocalized electronic space that enables long-range electronic interactions and multicenter synergistic coupling. This electronic synergy markedly strengthens conduction loss and dipolar polarization, delivering a minimum reflection loss of −68.78 dB and an effective absorption bandwidth of 6.00 GHz at a low loading of 6 wt%. Notably, Fe_{AC} exhibits a thermodynamically preferred adsorption toward Cl^-, generating locally enriched negative-charge regions that mitigate direct ionic attack on atomically dispersed Fe_{SA} sites and thereby suppress corrosion-induced performance degradation. In addition, the absorber film demonstrates mechanical flexibility and thermal insulation, highlighting its potential for durable and high-efficiency maritime EMW protection applications.

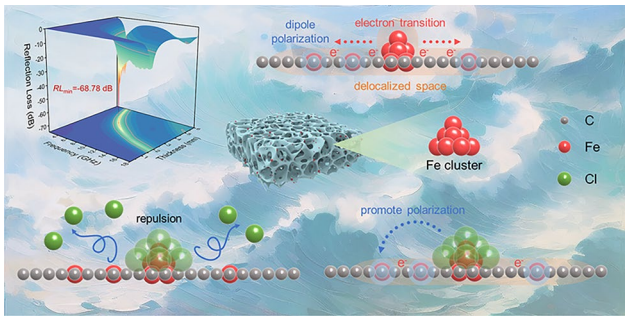

KEYWORDS Fe single atom; Fe cluster; Electromagnetic wave absorption; Electronic delocalization; Marine environment

✉ Pianpian Zhang, zhangpianpian1993@126.com; Yanan Yang, yangyanan310@163.com; Long Xia, xialonghit@gmail.com
[1] College of Materials Science and Engineering, Harbin Institute of Technology (Weihai), Weihai 264209, People's Republic of China
[2] Aerospace Science and Industry Wuhan Magnetism-Electron Co., Ltd, Wuhan 430074, People's Republic of China

Published online: 11 May 2026

Shanghai Jiao Tong University Press

Springer

1 Introduction

With the rapid development of wireless communication, marine exploration, and radar detection technologies, the escalating complexity of the marine electromagnetic environment has become a pivotal challenge restricting the performance of maritime systems [1, 2]. In particular, stealth technologies that evade radar detection are indispensable for augmenting the survivability and strategic deterrence of naval vessels and maritime aircraft, thereby necessitating the development of high-performance electromagnetic wave (EMW) absorbing coatings [3]. Distinct from terrestrial scenarios, marine service environments are characterized by high humidity and salinity, imposing stringent requirements on the long-term functional stability of EMW absorbers and their ability to maintain effective radar cross-section (RCS) suppression under harsh conditions [4, 5].

In recent years, EMW absorbers have evolved from conventional magnetic-metal to carbon, polymers, 2D materials, and multiscale composites, enabling notable progress in impedance matching and multi-mechanism loss coupling. Nevertheless, simultaneously achieving "thin, lightweight, broadband, and strong" absorption remains difficult, mainly due to low active-site utilization and limited structural/interfacial tunability, which constrain both absorption efficiency and rational design. In this context, single-atom (SA) absorbers have attracted significant attention owing to their maximum atomic utilization, well-defined coordination structures, and tunable electronic properties [6–8]. Atomically dispersed active sites facilitate strong dipole polarization and efficient dielectric loss, offering a promising pathway toward lightweight and high-efficiency absorbers [9–12]. However, the highly localized electronic states associated with isolated atoms, while beneficial for polarization loss, inevitably limit long-range charge transport and electron hopping processes, thereby restricting the synergistic activation of multiple EMW loss mechanisms. Moreover, under marine environments, isolated atoms are vulnerable to aggregation and competitive coordination with aggressive Cl^-, leading to severe poisoning of SA sites, substantially limiting SA absorber practical application in marine scenarios [13–16]. To enhance the stability of SA absorbers, multiple anti-corrosion strategies have been proposed, including protective encapsulation, defect engineering, and alloying. Despite the extensive efforts devoted to stabilizing single-atom absorbers, it should be noted that most existing strategies fundamentally rely on passive protection of isolated sites [17, 18]. Specifically, protective encapsulation suppresses moisture and ion attack but often compromises impedance matching and dielectric loss efficiency, while defect engineering mitigates corrosive ion adsorption at the expense of disrupting conductive networks [19–25]. Alloying can improve chemical stability, yet sacrifice atomic utilization and undermine the intrinsic advantage of atomic dispersion [26, 27]. As a result, such passive stabilization strategies inherently constrain charge transport and polarization dynamics, making it increasingly difficult to simultaneously realize environmental robustness and high electromagnetic energy dissipation. Under marine conditions dominated by aggressive Cl^- species, the degradation of SA absorbers is not governed solely by local coordination instability, but also by the absence of effective charge redistribution pathways capable of diverting corrosive ions away from atomically dispersed active sites. This intrinsic limitation suggests that stabilization of single atoms alone may be insufficient to overcome the long-term corrosion performance trade-off. Motivated by these considerations, introducing auxiliary functional units that can actively regulate local electronic environments and ion adsorption behavior emerges as a rational strategy to reconcile efficient EMW attenuation with environmental durability.

Herein, we report a Fe atomic cluster (Fe_{AC})–Fe single-atom (Fe_{SA}) synergistic absorber (NC-Fe_{AC2}) designed to enhance EMW dissipation through multiscale electronic cooperation, while simultaneously exhibiting improved tolerance toward moisture and marine corrosion [28, 29]. Anchoring Fe_{SA} in proximity to preferentially active Fe_{AC} enables electronic modulation via charge delocalization, thereby reinforcing local structural stability and facilitating electron hopping within the conductive network by lowering interfacial charge transfer barriers. Notably, Fe_{AC} exhibits a thermodynamic preference for Cl^- adsorption, enabling preferential capture of Cl^- and generating locally enriched negatively charged regions, and this repulsion effect effectively shields single-atom sites from direct Cl^- attack [30]. Unlike conventional passive protection strategies, the AC-SA synergistic strategy provides active protection by redistributing charges and selectively binding corrosive ions. Consequently, it preserves atomic dispersion and activity while harmonizing polarization and conductive loss mechanisms to enhance EM energy dissipation. This work deepens the

https://doi.org/10.1007/s40820-026-02210-y

understanding of the interplay between electronic synergy, EMW absorption performance, and environmental stability in SA-based absorbers and offers a feasible design paradigm for next-generation EMW absorbing materials.

2 Experimental Section

2.1 Materials

Dopamine hydrochloride ($C_8H_{11}NO_2$·HCl, 98%), sodium chloride (NaCl, 99.5%), iron(II) chloride tetrahydrate ($FeCl_2$·$4H_2O$, 98%), hydrochloric acid (HCl, 36–38%), and ethyl alcohol (CH_3CH_2OH, 99.8%) were both purchased from Shanghai Maclin Biochemical Technology Co., Ltd (Shanghai, China).

2.2 Preparation of NC, NC-Fe_{ACX} and NC-Fe_{NP}

2.2.1 Preparations of the NC-Fe_{ACX}

A mixture of 5.0 g of NaCl, 0.5 g of dopamine hydrochloride, and 0.2 g of $FeCl_2$·$4H_2O$ was dissolved in 100 mL of deionized water and stirred for 24 h to obtain a homogeneous solution. The above solution was then frozen with liquid nitrogen and freeze-dried at − 60 °C and 0.1 Pa for 3 days. The as-prepared powder was calcined at 700, 800, and 900 °C for 3 h under a nitrogen atmosphere with a heating rate of 3 °C min^{-1}, followed by etching in 50 mL of 2 M HCl solution at 60 °C for 24 h and repeated washing with deionized water to remove the NaCl template. Finally, the sample was dried at 80 °C for 24 h in a convection oven and the product treated at 700, 800, and 900 °C was denoted as NC-Fe_{AC1}, NC-Fe_{AC2}, and NC-Fe_{AC3}, respectively.

2.2.2 Preparations of the NC

5.0 g of NaCl and 0.5 g of dopamine hydrochloride were dissolved in 100 mL of deionized water, and the resulting solution was stirred for 24 h to form a homogeneous mixture. The above solution subsequently rapidly frozen in liquid nitrogen and freeze-dried at − 60 °C and 0.1 Pa for 3 days. The obtained powder was then calcined at 800 °C for 3 h under a nitrogen atmosphere with a heating rate of 3 °C min^{-1}, followed by repeated washing with deionized water until the NaCl template was completely removed. Finally, the sample was dried at 80 °C for 24 h in a convection oven and the product was denoted as NC.

2.2.3 Preparations of the NC-Fe_{NP}

5.0 g of NaCl, 0.5 g of dopamine hydrochloride, and 0.2 g of $FeCl_2$·$4H_2O$ were dissolved in 100 mL of deionized water and stirred for 24 h until a uniform solution was obtained. The mixture was then rapidly frozen using liquid nitrogen and freeze-dried at − 60 °C and 0.1 Pa for 3 days. The resulting powder was calcined at 900 °C for 3 h under a nitrogen atmosphere with a heating rate of 3 °C min^{-1}, after which it was repeatedly washing with deionized water to remove the NaCl template. Finally, the sample was dried at 80 °C for 24 h in a convection oven and the obtained product was denoted as NC-Fe_{NP}.

2.3 Characterization

The morphology, microstructure, and elemental distribution of the samples were investigated by scanning electron microscopy (SEM, MERLIN Compact, Zeiss) and transmission electron microscopy (TEM, FEI Talos F200x, Thermo Fisher). Atomic distribution and coordination environments were further analyzed by double spherical aberration-corrected transmission electron microscope (double-Cs TEM, JEM-ARM300F, JEOL). The phase composition was determined by X-ray diffraction (XRD, Cu Kα, $\lambda = 1.5418$ Å) with a scanning speed of 10° min^{-1} in the range of 3°–90°. Surface elemental valence states were analyzed by X-ray photoelectron spectroscopy (XPS, ESCALAB Xi+, Thermo Fisher) with Al Kα X-ray source. X-ray absorption near-edge structure (XANES) and extended X-ray absorption fine structure (EXAFS) spectra at the Fe K-edge were recorded in fluorescence mode. Raman spectroscopy (Renishaw, In Via, $\lambda = 523$ nm) was used to probe structural features and defect states of the samples. Chemical bonds and functional groups of the samples were analyzed by Fourier-transform infrared spectroscopy (FT-IR, TENSOR II, Bruker). The thermal conductivity of the samples was measured using a thermal constants analyzer (Hot Disk TPS2500S). To evaluate electromagnetic properties, coaxial ring (outer diameter 7.00 mm, inner diameter 3.04 mm) was fabricated by

dispersing 6 wt% of the samples into paraffin. The complex permittivity and permeability were measured multiple times in the range of 2–18 GHz using a vector network analyzer (E8363B, Agilent).

3 Results and Discussion

3.1 Design Principle of NC-Fe_{ACX} and Structural Characterizations

To elucidate the intrinsic mechanism by which long-range electron migration between Fe_{AC} and Fe_{SA} enhances EMW absorption, first-principles calculations were performed to evaluate the electronic structure and spatial charge distribution of three models: isolated Fe single atoms (Fe_{SA}), coexisting Fe single atoms and clusters (Fe_{SA-AC}), and Fe clusters (Fe_{AC}) (Figs. 1a–c). In the Fe_{SA} model (Fig. 1d), the charge density difference analysis reveals a continuous charge accumulation zone along the Fe–N bond, accompanied by the delocalization of electrons from the bonding region to the periphery, forming a spatially symmetrical electron transfer feature. This phenomenon stems from the dominant σ-π conjugation hybridization between the pyridine nitrogen's p_z orbital and Fe's d_{xz}/d_{yz} orbitals, and the effective overlap of p—d orbitals not only promotes the localized accumulation of electrons in the bonding region but also drives the symmetrical diffusion of electrons into the space outside the bond due to the delocalization characteristic of the conjugated system. Consistent with this, the projected density of states (PDOS) shows narrow and discrete d orbital peaks near the Fermi level, with a significant downward shift of the d orbital center (ε_d) and a low density of states at the Fermi level (Fig. 1g), indicating that in the Fe-N_4 coordination environment, d orbital electrons exhibit a clear localized feature due to the localization of orbital hybridization, and the range of electron delocalization is limited. In contrast, in the Fe_{AC} model (Fig. 1e), Fe–Fe atoms form bonding through strong d—d orbital overlap, with significant orbital wave function overlap leading to an expanded range of electron delocalization within the Fe aggregate; the charge redistribution is mainly concentrated within the Fe cluster and at the interface between the cluster and the carrier, reflecting a weakened orbital hybridization between the aggregate and the carrier, and the electron delocalization path is more confined within the metal cluster. Correspondingly, the d orbital broadening is the greatest, with a significant density of states and continuous d orbital occupation at the Fermi level (Fig. 1h), demonstrating typical metallic electron delocalization behavior, and electrons have high transportability [31]. Notably, in the Fe_{SA-AC} model (Fig. 1f), there is a cooperative coupling effect between isolated Fe single-atom sites and Fe clusters: The π-conjugated carbon carrier and the coordinating N atoms connecting the two form a continuous orbital conjugation network, creating a long-range polarization channel that mediates the long-range charge redistribution process involving the substrate. Driven by the local potential gradient and the mismatch of density of states, the d electrons of the Fe cluster preferentially inject into the conjugated system of the carbon carrier through orbital overlap and then migrate to the Fe single-atom sites via the p orbitals of the N atoms. The PDOS results (Fig. 1i) further confirm that in this model, the d orbital bandwidth is moderately broadened, ε_d is shifted upward, and the contribution of d orbital density of states near the Fermi level (especially the d_{xz}/d_{yz} orbitals) is significantly enhanced, indicating an expanded range of electron delocalization, a reduced energy barrier for interorbital transitions, and a significantly improved electron transport capability. At the same time, the Fe cluster acts as an electron buffer center, achieving long-range electron transfer and multi-site cooperative migration through dynamic regulation of interface charges [32–34]. Therefore, constructing a composite system where single atoms and clusters coexist can significantly enhance electron mobility and control dielectric response by optimizing electron delocalization paths and orbital transition efficiency, providing a key guarantee for efficient attenuation of EM waves. Guided by simulation results, a series of NC-Fe_{ACX} absorbers with tunable Fe_{AC} sizes were rationally synthesized. As illustrated in Fig. 1j, dopamine hydrochloride and sodium chloride were dissolved in deionized water, followed by the introduction of ferrous chloride to form a homogeneous precursor solution. During freeze-drying, dopamine hydrochloride self-polymerized on the sodium chloride hard template (Fig. S1), where nitrogen atoms facilitated the uniform dispersion of Fe atoms. Subsequent pyrolysis under a nitrogen atmosphere, followed by acid leaching, produced N-doped absorbers containing homogeneously dispersed Fe_{SA} and Fe_{AC}.

https://doi.org/10.1007/s40820-026-02210-y

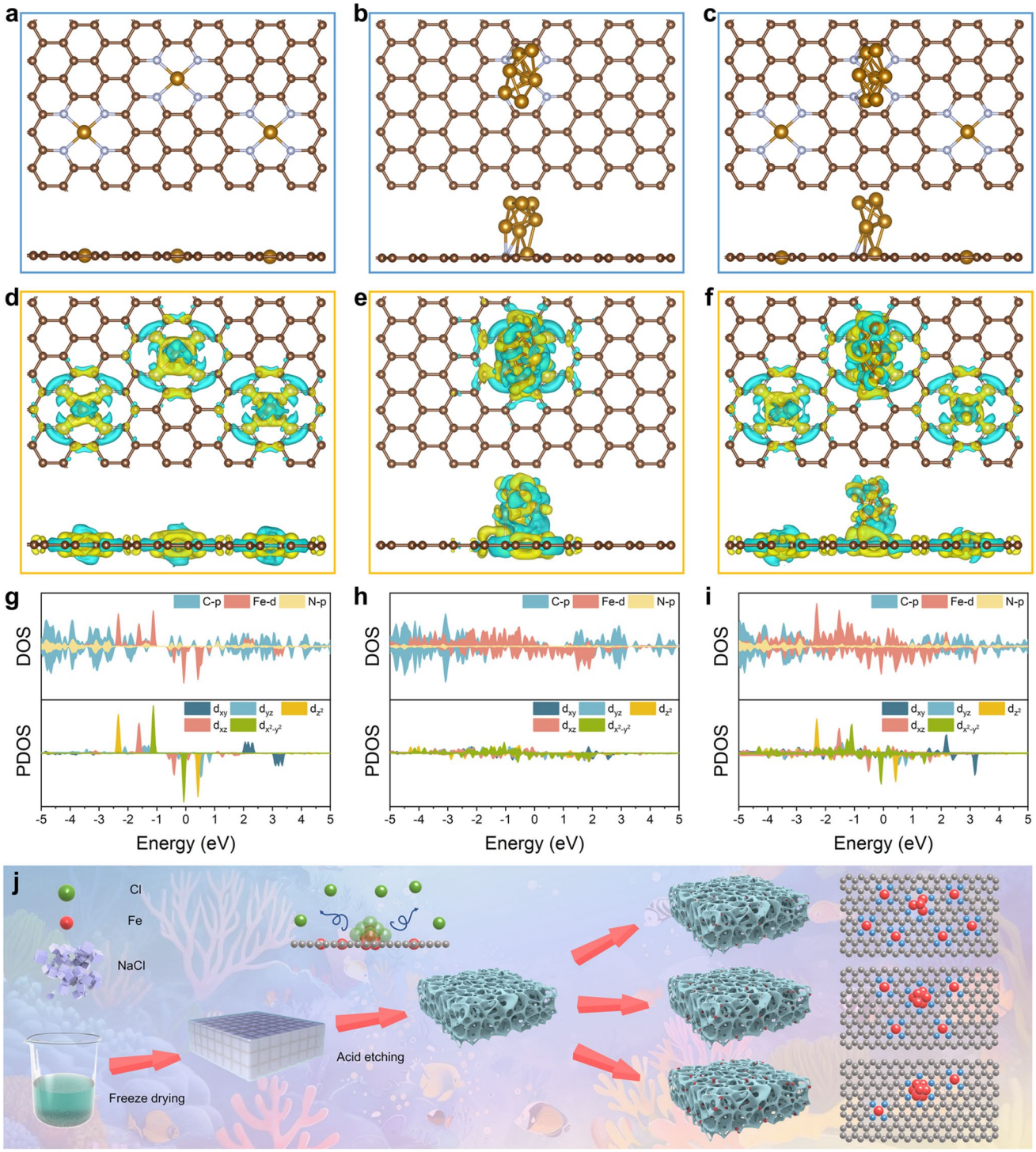

Fig. 1 Model of **a** Fe_{SA}, **b** Fe_{AC}, and **c** Fe_{AC-SA} material. Charge density difference of **d** Fe_{SA}, **e** Fe_{AC}, and **f** Fe_{AC-SA} material. (The charge accumulation and depletion regions are represented by yellow and cyan, respectively.) Projected density of state (PDOS) and DOS of Fe *d* band in **g** Fe_{SA}, **h** Fe_{AC}, and **i** Fe_{AC-SA} material. **j** Schematic illustration of the synthesis process of NC-Fe_{ACX}

Figure 2a presents the X-ray diffraction (XRD) patterns of NC, NC-Fe_{ACX}, and NC-Fe_{NP}, which display two broad amorphous peaks at ~22° and ~44°, corresponding to the (002) and (101) planes of graphitic carbon. In addition, NC-Fe_{NP} exhibits the diffraction peaks at ~44.7° ~65.1°, and ~82.3°, assigned to metallic Fe (JCPDS No. 06-0696) [35], indicating the aggregation of Fe nanoparticles in NC-Fe_{NP}, whereas no such peak is observed in NC-Fe_{ACX}. The surface chemical composition (Figs. S8-S10) and bonding configurations were further probed via X-ray photoelectron spectroscopy (XPS). The N 1*s* spectra (Fig. 2b) can be deconvoluted into pyridinic N (398.4 eV), pyrrolic N/M–N (399.8 eV), graphitic N (401.4 eV), and oxidized N (403.3 eV) [36]. Notably, the relative contribution of pyrrolic N/M–N increased significantly with the incorporation of Fe atoms, indicating that N species play a crucial role in anchoring Fe atoms. The Fe 2*p* spectrum (Fig. 2c) of NC-Fe_{ACX} shows Fe^{2+} $2p_{3/2}$ (710.3 eV) and Fe^{2+} $2p_{1/2}$

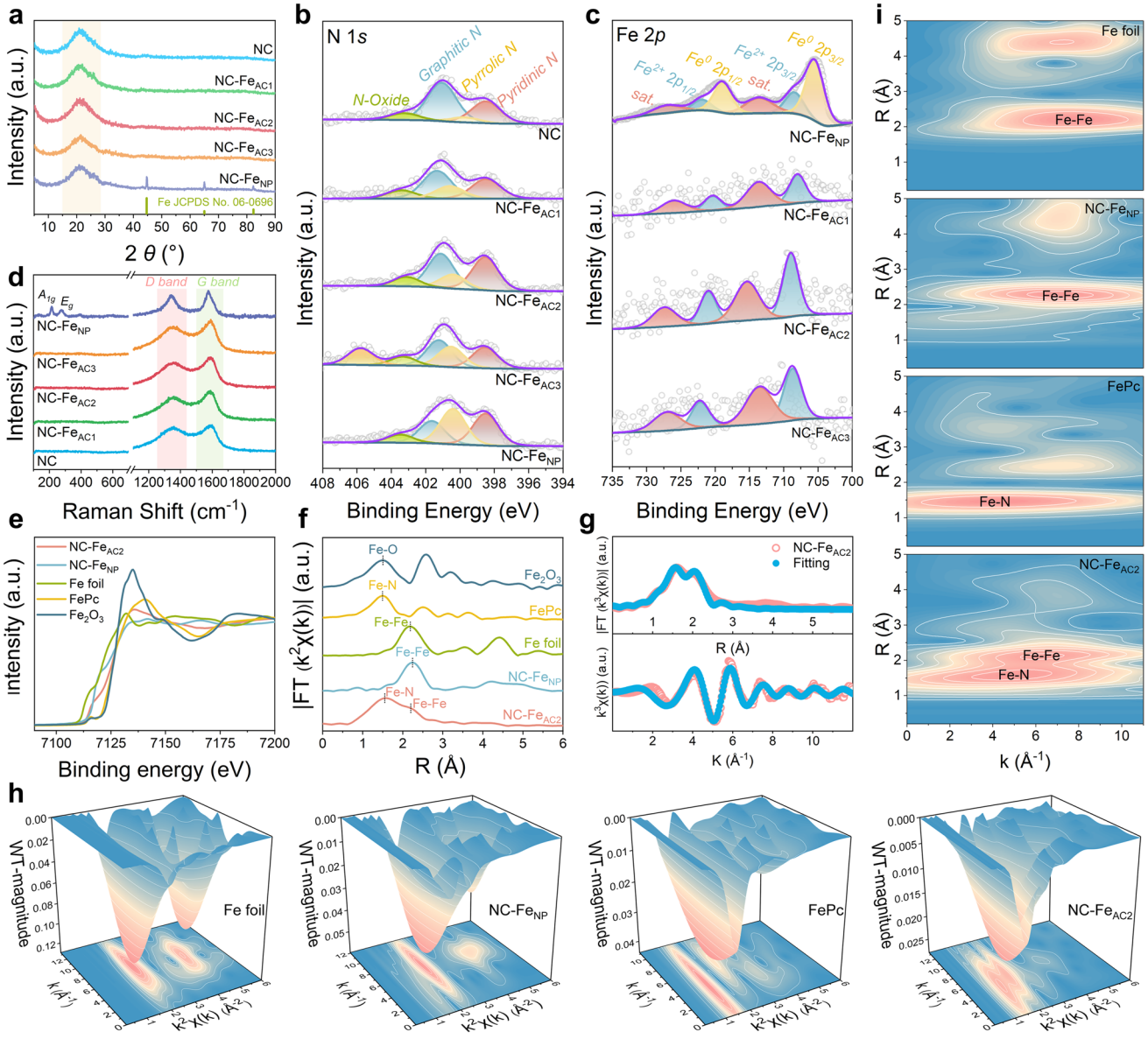

Fig. 2 **a** XRD pattern of NC, NC-Fe_{ACX}, and NC-Fe_{NP}. **b** N 1*s*, **c** Fe 2*p* high-resolution XPS spectra, and **d** Raman spectra of NC, NC-Fe_{ACX}, and NC-Fe_{NP}. **e** Fe K-edge XANES spectra and **f** Fe K-edge k.^{2}-weighted EXAFS spectra of NC-Fe_{AC2}, NC-Fe_{NP}, Fe foil, FePc, and Fe_2O_3. **g** Fitted Fe K-edge EXAFS curve of NC-Fe_{AC2} in the *k* and *R* space. **h** WT-EXAFS spectra and **i** projection of Fe foil, NC-Fe_{NP}, FePc, and NC-Fe_{AC2}

https://doi.org/10.1007/s40820-026-02210-y

(723.4 eV) peaks with two satellite peaks. In contrast, NC-Fe_{NP} exhibits additional metallic Fe^0 $2p_{3/2}$ (707.3 eV) and Fe^0 $2p_{1/2}$ (720.4 eV) peaks, demonstrating that Fe atoms in NC-Fe_{ACX} exist exclusively as isolated Fe_{SA} and Fe_{AC} without aggregation into nanoparticles [37]. The FT-IR spectra exhibit characteristic bands at 3600–3000, 1250–1050, and 1650–1550 cm^{-1}, which are assigned to O–H/N–H, C–O–C, and C=C/C=N stretching vibrations in NC-Fe_{ACX} and NC-Fe_{NP}, respectively. Notably, the functional groups-related bands gradually weaken from NC-Fe_{AC1} to NC-Fe_{AC3}, indicating progressively enhanced deoxygenation/dehydrogenation upon more severe thermal treatment (Fig. S11). Raman spectra (Fig. 2d) reveal the characteristic D (~ 1350 cm^{-1}) and G (~ 1580 cm^{-1}) bands of carbon, corresponding to defect-induced vibrations and the ordered vibrations of sp^2 carbons, respectively [38]. The I_D/I_G ratios follow the order: NC (0.73) < NC-Fe_{AC1} (1.01) < NC-Fe_{AC2} (1.03) < NC-Fe_{AC3} (1.04) < NC-Fe_{NP} (1.10), indicating that the incorporation of Fe atoms introduces additional defects (Fig. S12). Specifically, Fe_{AC} generate coordination and boundary sites on the support that distort the local carbon structure, whereas larger nanoparticles exacerbate interfacial damage and local oxidation, thereby elevating the defect density. In addition to the D and G bands, the NC-Fe_{NP} sample exhibits distinct Fe–O Raman peaks at 225 cm^{-1} (A_{1g}, symmetric stretching vibration of O along the Fe–O bond), 247, and 293 cm^{-1} (E_g, bending and shear vibrations of O perpendicular to the Fe–O bond), which are attributed to the oxidation of Fe nanoparticles with high surface energy [39–41]. Extended X-ray absorption fine structure (EXAFS) and X-ray absorption near-edge structure (XANES) were performed to elucidate the fine structure and coordination environment of NC-Fe_{AC2} and NC-Fe_{NP}. As shown in the Fe K-edge XANES spectra (Fig. 2e), the absorption edge of NC-Fe_{AC2} lies between Fe foil and Fe_2O_3, corresponding to an oxidation state between 0 and + 3. Moreover, NC-Fe_{NP} exhibits an edge position close to Fe foil, consistent with a near-zero valence state. Notably, the absorption edge of NC-Fe_{AC2} shows a slight shift relative to FePc (~ 7115 eV), implying that the introduction of Fe_{AC} induces distortions in the coordination structure of Fe_{SA} sites (Fe-N_4) [36, 42]. The k^2-weighted Fourier transform (FT) of the Fe K-edge EXAFS spectra (Fig. 2f) further reveals the local coordination environments of Fe atoms. NC-Fe_{NP} shows a dominant peak at ~ 2.2 Å, nearly identical to Fe foil, corresponding to the first-shell Fe–Fe scattering path and confirming the presence of Fe nanoparticles. In contrast, NC-Fe_{AC2} exhibits a main peak at ~ 1.5 Å, consistent with FePc and attributable to the first-shell Fe–N scattering path, while a secondary peak at ~ 2.2 Å reveals the coexistence of Fe–Fe bonds on the support [43, 44]. Quantitative EXAFS fitting in k and R space confirms the coexistence of isolated Fe-N_4 sites and Fe_{AC} sites in the NC-Fe_{AC2} (Fig. 2g). Wavelet transform (WT) of EXAFS spectra further identifies the Metal-N and Metal–Metal coordination paths (Figs. 2h, i). FePc and Fe foil show a single maximum at ~ 4.0 and ~ 7.2 $Å^{-1}$, assigned to Fe–N and Fe–Fe paths, respectively. In contrast, NC-Fe_{AC2} exhibits two distinct maxima at ~ 4.2 and ~ 6.4 $Å^{-1}$, corresponding to Fe–N and Fe–Fe paths, significantly different from the WT signals of FePc and Fe foil [45, 46]. This divergence indicates that electron delocalization effect between Fe_{SA} sites and Fe_{AC} induces distortions in the local coordination environment, thereby facilitating polarization loss.

Scanning electron microscopy (SEM) and transmission electron microscopy (TEM) revealed that NC-Fe_{ACX} possessed a smooth three-dimensional (3D) porous coral-like morphology, indicating the homogeneous dispersion of Fe species (Figs. 3a–b and S2–S6). In contrast, the non-acid-treated NC-Fe_{NP} sample (Figs. 3c, d) exhibited extensive Fe nanoparticles aggregation with sizes below 10 nm induced by thermal migration of Fe atoms. To further elucidate the distribution states of Fe_{SA} and Fe_{AC} within the support, aberration-corrected high-angle annular dark-field scanning transmission electron microscopy (HAADF-STEM) was employed for atomic-scale analysis of NC-Fe_{ACX}. As shown in Figs. 3e–h, Fe_{AC} surrounded by Fe_{SA} sites were uniformly distributed across the support. With increasing calcination temperature, the size of Fe_{AC} gradually increased, accompanied by a progressive decrease in the number of Fe_{SA} sites (Fig. S7). The 3D visualization fitting (Fig. 3g) vividly illustrated a cooperative island–archipelago configuration formed by Fe_{SA} and Fe_{AC}. Furthermore, energy-dispersive X-ray (EDX) elements mapping confirmed the homogeneous distribution of C, N, O, and Fe in NC-Fe_{ACX} (Fig. 3i), with no Fe nanoparticles aggregation.

3.2 Electromagnetic Performance and Mechanism

To evaluate the EMW absorption performance, the intrinsic EM parameters—relative complex permittivity ($\varepsilon_r = \varepsilon' - j\varepsilon''$)

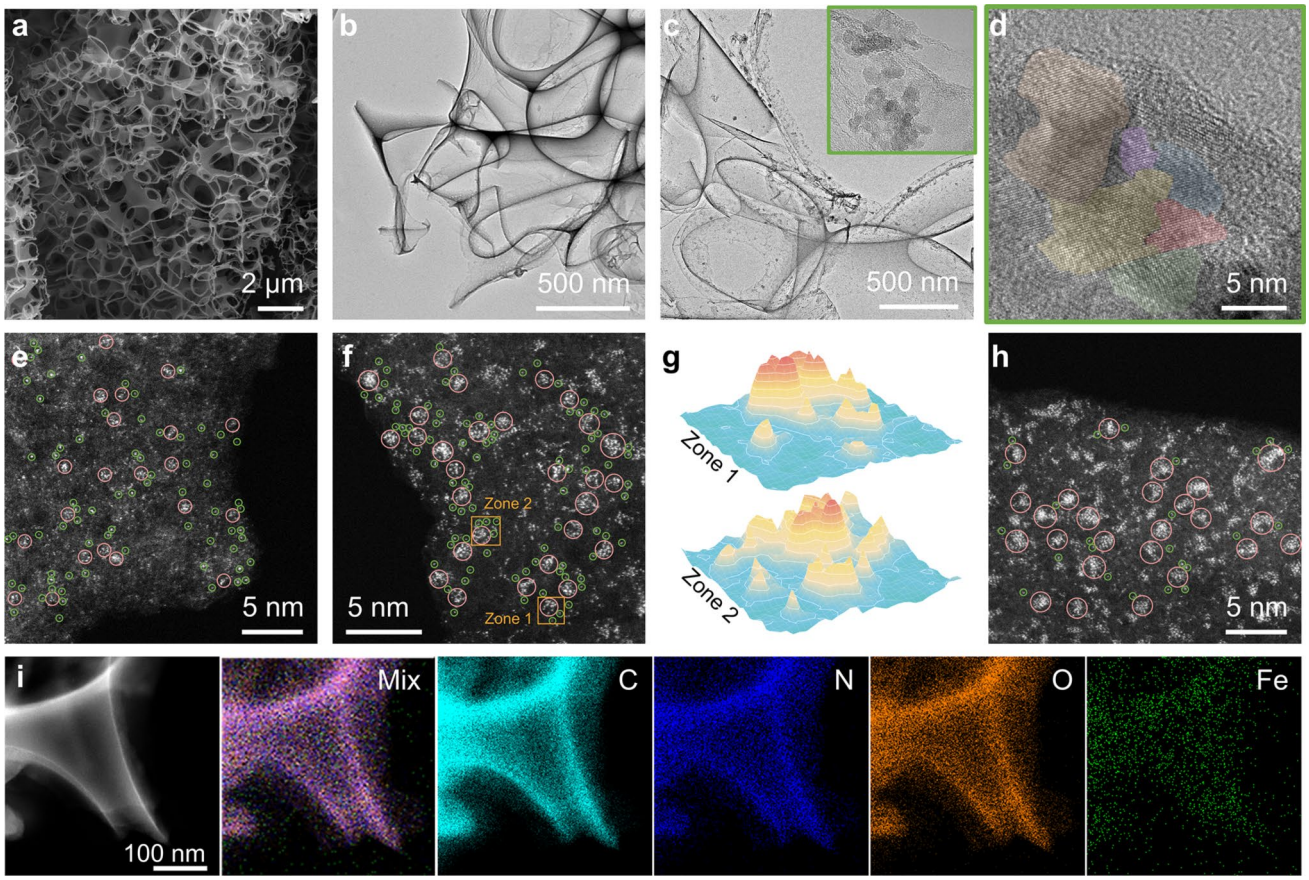

Fig. 3 **a** SEM image of NC-Fe_{AC2}. **b** TEM image of NC-Fe_{AC2}. **c** TEM and **d** HRTEM image of NC-Fe_{NP}. AC-HAADF-STEM image of **e** NC-Fe_{AC1}, **f** NC-Fe_{AC2}, and **h** NC-Fe_{AC3}. **g** 3D fitting image of zones 1 and 2 in NC-Fe_{AC2}. **i** EDX element mapping image of NC-Fe_{AC2}

and relative complex permeability ($\mu_r = \mu' - j\mu''$)—were measured at a filler loading of 6 wt%. As shown in Figs. 4a and S13, the μ' and μ'' values of NC and NC-Fe_{ACX} are close to 1 and 0, respectively, indicating the absence of magnetism and confirming the uniform dispersion of Fe atoms consistent with the SEM and TEM observations. In contrast, the μ' and μ'' values of NC-Fe_{NP} exceed 1 and 0, respectively, indicating its magnetic loss capability [47]. The magnetic hysteresis loops (Fig. 4b) further reveal the magnetic distinction of NC-Fe_{AC2} and NC-Fe_{NP}. NC-Fe_{AC2} exhibits an almost linear hysteresis response through the origin, indicating negligible variation in magnetic induction ($\Delta B \approx 0$) under an external magnetic field, whereas NC-Fe_{NP} shows a smooth superparamagnetic "S"-shaped loop with nearly zero remanence and coercivity [48]. This behavior indicates that the Fe nanoparticles have a single-domain structure where magnetic moments randomly flip under thermal fluctuations, thereby eliminating remanence and coercivity at the macroscopic scale (Figs. 3c, d). Moreover, the saturation magnetization (Ms) of NC-Fe_{NP} (13.87 emu g^{-1}) significantly exceeds that of NC-Fe_{AC2} (0.20 emu g^{-1}), further corroborating its superior magnetic loss capability. The low-frequency resonance peaks of the C_0 parameter are attributed to natural resonance and exchange resonance in the 2–18 GHz range, while the approach of C_0 toward zero at higher frequencies suggests that eddy current loss occupies the dominant mechanism (Fig. 4c). The permittivity of the samples reflects the dielectric behavior under EMW. As shown in Figs. 4d and S14, the real (ε') and imaginary (ε'') parts of permittivity represent energy storage and dissipation, respectively. All samples exhibit a frequency-dependent decrease in permittivity due to the intrinsic frequency

 https://doi.org/10.1007/s40820-026-02210-y

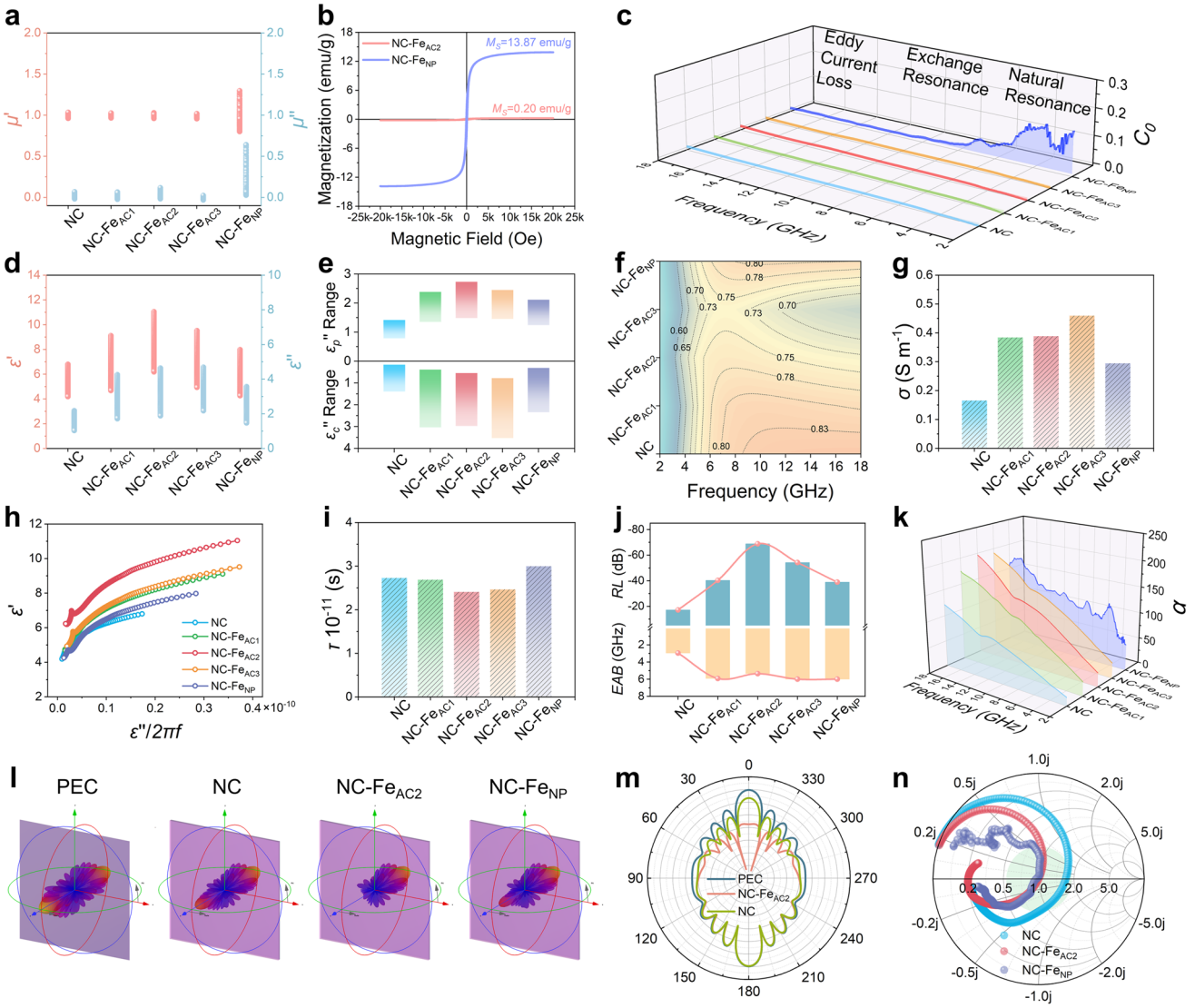

Fig. 4 **a** Permeability ranges of NC, NC-Fe$_{ACX}$, and NC-Fe$_{NP}$. **b** Hysteresis loops of NC-Fe$_{AC2}$ and NC-Fe$_{NP}$. **c** The C_0 values, **d** permittivity ranges, **e** ε''_c and ε''_p ranges, **f** contribution of polarization loss to dielectric loss, **g** σ values, **h** ε'-$\varepsilon''/2\pi f$ curves, **i** τ values, **j** *RL* and *EAB* values, and **k** α values of NC, NC-Fe$_{ACX}$, and NC-Fe$_{NP}$. **l** 3D radar wave scattering signal of PEC, NC, NC-Fe$_{AC2}$, and NC-Fe$_{NP}$. **m** RCS simulation curves, and **n** smith chart of NC, NC-Fe$_{AC2}$, and NC-Fe$_{NP}$

dispersion effect. With the incorporation of Fe$_{SA}$, Fe$_{AC}$, and Fe$_{NP}$, the ε' values of NC, NC-Fe$_{AC1}$, NC-Fe$_{AC2}$, NC-Fe$_{AC3}$, and NC-Fe$_{NP}$ oscillate within the ranges of 6.80–4.19, 9.11–4.68, 11.04–6.19, 9.52–4.93, and 7.97–4.26, respectively, while the ε'' values fluctuate within 2.18–1.03, 4.25–1.71, 4.63–1.88, 4.69–2.17, and 3.56–1.47, respectively. Compared with NC, both NC-Fe$_{ACX}$ and NC-Fe$_{NP}$ exhibit higher ε' and ε'' values, indicative of enhanced dielectric properties, as further corroborated by the dielectric loss tangent (tan δ_ε). To better distinguish the contributions of conduction loss (ε''_c) and polarization loss (ε''_p), the permittivity was quantitatively fitted using the least-squares method (Figs. 4e, S15, and S16) [49]. The ε''_c values of NC-Fe$_{ACX}$ are significantly higher than those of NC (1.40—0.16), consistent with the conductivity trend (Fig. 4g): NC-Fe$_{AC3}$ (0.4597 S m^{-1}) > NC-Fe$_{AC2}$ (0.3886 S m^{-1}) > NC-Fe$_{AC1}$ (0.3843 S m^{-1}) > NC-Fe$_{NP}$ (0.2945 S m^{-1}) > NC (0.1657 S m^{-1}). These results demonstrate that Fe$_{AC}$ and Fe$_{SA}$ sites markedly enhance the electrical conductivity of the samples. This improvement

originates from the electron delocalization space generated between Fe_{AC} and Fe_{SA}, which promotes electron hopping in the support, optimizes the conductive network of NC-Fe_{ACX}, and thereby strengthens conduction loss. Meanwhile, ε''_p reveals a volcano-like trend with increasing Fe_{AC} size. In the Fe SA model, the pyridine N p_z orbitals form σ-π conjugated hybridization with the Fe d_{xz}/d_{yz} orbitals, and the accumulation and symmetrical delocalization of charges along the Fe–N bond form a directional dipole moment; when Fe_{AC} is introduced, the cooperative effect of the cluster and single atom distorts the symmetrical charge distribution of the Fe-N_4 environment, intensifying the dipole polarization strength of the Fe–N bond, thereby enhancing the polarization loss (Fig. 4f). However, further increasing the size of Fe_{AC} causes the space hindrance effect of the clusters to intensify, thereby occupying the anchoring sites of the Fe_{SA}, resulting in a synchronous decrease in the regional density of Fe_{AC} and Fe_{SA} on the π-conjugated carbon carrier surface. The decrease in site density will directly disrupt the effective overlap between the 3*d* orbitals of Fe_{SA} and the d-bands of Fe_{AC}, hindering the delocalized transmission of interface electrons, and causing the electron state density distribution near the Fermi level to become discrete, unable to form a continuous polarization charge enrichment area. This not only weakens the cooperative regulatory effect of Fe_{AC} and Fe_{SA} sites on dielectric polarization, but is also highly consistent with density dependence of the "cluster-single atom" cooperative polarization channel in the $Fe_{SA\text{-}AC}$ model—that is the polarization relaxation efficiency is positively correlated with the interface electron coupling density of the monomer–cluster. In summary, the synergistic effect of Fe_{SA} and size-controllable Fe_{AC} achieves a dynamic balance between conductive loss and polarization loss: Fe_{AC} enhances electronic conduction through *d*—*d* orbital delocalization, while Fe_{SA} regulates directional polarization via σ-π hybridization. The orbital conjugation network formed by the two promotes long-range charge migration and multi-site cooperative response (Fig. S17). This synergistic regulation mechanism of electronic delocalization and orbital polarization provides a key guarantee for optimizing dielectric response and enhancing electromagnetic wave attenuation efficiency. According to the Debye theory, the ε'-ε'' relationship of samples reveals multiple Cole–Cole semicircles accompanied by a linear tail, indicating that both conduction loss and multiple polarization losses contribute to the EMW absorption (Fig. S18). The relaxation time (τ) represents the characteristic timescale for a system to recover from non-equilibrium to equilibrium state, which quantifies the response of dipoles or charges to an alternating EM field and serves as a critical parameter of polarization loss capability. As shown in the ε'-$\varepsilon''/2\pi f$ plots, the relaxation times follow the order (Figs. 4h, i): NC-Fe_{NP} (3.00×10^{-11} s) > NC (2.73×10^{-11} s) > NC-Fe_{AC1} (2.69×10^{-11} s) > NC-Fe_{AC3} (2.47×10^{-11} s) > NC-Fe_{AC2} (2.41×10^{-11} s). Notably, NC-Fe_{AC2} exhibits the shortest relaxation time, confirming its superior polarization loss capability by enabling the most efficient conversion of EM energy into heat. Moreover, this ultrashort relaxation time further demonstrates that the delocalized space formed between Fe_{SA} and Fe_{AC} efficiently promotes electron hopping. In the coexisting Fe_{SA}-Fe_{AC} system, the Fe_{SA} *3d* orbitals hybridize with the carbon support *2p* π orbitals, while Fe_{AC} *3d* orbitals weakly couple with the carbon orbitals, generating multicenter orbital overlap between Fe_{SA} and Fe_{AC} via the carbon support. This orbital coupling network facilitates electron delocalization among Fe_{SA}, Fe_{AC}, and carbon, which significantly enhances both conduction and polarization loss. The EMW absorption performance was systematically assessed by reflection loss (RL, where RL < − 10 dB corresponds to 90% EMW absorption) and effective absorption bandwidth (EAB). The pristine NC sample without Fe_{SA} or Fe_{AC} exhibited poor performance, with an RL_{min} of − 17.17 dB and an EAB of 2.96 GHz at a thickness of 6.0 mm. With the incorporation of Fe_{SA} and Fe_{AC}, the absorption performance of NC-Fe_{ACX} was significantly enhanced. NC-Fe_{AC1} achieved an RL_{min} of − 40.27 dB at 6.0 mm and an EAB of 5.92 GHz at 2.5 mm, while NC-Fe_{AC2} demonstrated better performance, reaching an RL_{min} of − 68.78 dB at 3.8 mm and an EAB of 5.36 GHz at 2.1 mm. The performance enhancement can be ascribed to the size modulation of Fe_{AC}. Within the Fe_{SA}-Fe_{AC} system, appropriately sized Fe_{AC} provides an optimal balance between orbital hybridization and electron migration: Partially overlapping 3d orbitals generate quasi-continuous energy bands while retaining a high density of Fe_{SA} active sites. Such a configuration enables effective coupling of Fe_{AC} *3d* orbitals with both the carbon *2p* π orbitals and Fe_{SA} *3d* orbitals, thereby establishing a multicenter hybridization network. This structure promotes extensive electron delocalization and accelerates charge transfer among Fe_{SA}, Fe_{AC}, and the carbon support, thereby significantly enhancing both polarization and conduction loss. Notably, further growth of clusters slightly degraded the performance of NC-Fe_{AC3},

 https://doi.org/10.1007/s40820-026-02210-y

which showed an RL_{min} of − 54.16 dB at 3.5 mm and an EAB of 6.00 GHz at 2.4 mm. In contrast, substitution with Fe nanoparticles yielded only limited improvement, which NC-Fe_{NP} displays an RL_{min} of − 38.84 dB at 3.9 mm and an EAB of 6.00 GHz at 2.7 mm (Figs. S19, 20). Considering both the EAB-RL_{min} relationship (Fig. 4j) and attenuation constant (α), NC-Fe_{AC2} is identified as the optimal absorber, delivering the most efficient overall EMW absorption performance (Fig. 4k). The EMW absorption performance of absorbers depends on both attenuation capability and impedance matching. When the input impedance (Z_{in}) falls within the green circle of the Smith chart (Fig. 4n), the reflection coefficient remains in the optimal range, with the center point ($Z' = 1 + j0$) denoting perfect matching [50]. The upper and lower halves of the horizontal axis correspond to inductive and capacitive characteristics, and resonance occurs when the impedance curve intersects this axis. With increasing frequency, the impedance curves of NC, NC-Fe_{AC2}, and NC-Fe_{NP} shift from inductive to capacitive behavior. Notably, the impedance curve of NC-Fe_{AC2} passes directly through the center point ($Z' = 1 + j0$) and occupies the largest number of points within the green circle, evidencing its superior impedance matching. When Z_{in} approaches the impedance of free space ($0.8 < |Z_{in}/Z_0| < 1.2$), EMW can readily penetrate the absorber with minimal reflection. Consistently, NC-Fe_{AC2} exhibits the broadest red region (Fig. S23), while the correlation curves of reflection loss and impedance matching at different thicknesses are concentrated around $|Z_{in}/Z_0| = 1$, further confirming NC-Fe_{AC2} with the most favorable impedance matching (Fig. S24). The radar cross section (RCS) of samples was simulated using CST software to evaluate their practical application potential. A perfect electric conductor (PEC) substrate was coated with NC, NC-Fe_{ACX}, and NC-Fe_{NP}. As shown in the 3D radar reflection signals (Fig. 4l), absorbers could significantly reduce the scattering intensity, with NC-Fe_{AC2} exhibiting the lowest scattering signal. Furthermore, the RCS attenuation curves under varying 2D incidence angles (Figs. 4m and S25) further confirm this trend: NC-Fe_{AC2} (27.05 dB) > NC-Fe_{AC3} (16.95 dB) > NC-Fe_{AC1} (14.37 dB) > NC-Fe_{NP} (10.38 dB) > NC (6.38 dB). Among them, NC-Fe_{AC2} exhibits a substantially lower RCS value than other samples, which underscores its potential for practical applications at a 6 wt% filler loading.

3.3 Properties and Applications of Multifunctional Films

Charge density difference analysis and adsorption energy calculation reveal pronounced thermodynamic disparities in Cl^- binding among the Fe species. As shown in Fig. 5a, Cl^- adsorption on the Fe_{SA} site gives an adsorption energy of − 2.61 eV, whereas a substantially stronger interaction is obtained on the Fe_{AC} site with a more negative value of − 3.09 eV (Fig. 5b). Notably, when Fe_{SA} coexists with Fe_{AC}, the Cl^- adsorption energy on the Fe_{AC} domain further decreases to − 3.11 eV (Fig. 5c), evidencing a clear thermodynamic preference of Cl^- for Fe_{AC}. Consistent with this prediction, the attenuation of EMW absorption performance in 3.5 wt% NaCl solution follows the order: NC-Fe_{AC1} (45.67%) > NC-Fe_{NP} (34.68%) > NC-Fe_{AC3} (24.65%) > NC-Fe_{AC2} (4.64%), indicating that the introduction of appropriately sized Fe_{AC} significantly enhances the resistance of absorbers against Cl^- corrosion (Figs. 5d and S33–S36). This improvement arises from the preferential accumulation of Cl^- on Fe_{AC}, which generates a locally enriched negative charge region and thereby effectively reduces the concentration of free Cl^- near Fe_{SA}, thus mitigating the poisoning effect and enhancing the absorption stability of absorbers in marine environments. The polarization capability is improved after NaCl treatment due to Cl^--induced local charge redistribution in Fe_{AC}, which generates additional dipoles and promotes polarization loss (Figs. 5e, f and S27–S32). To validate the EMW absorption performance under practical conditions, bow-shaped method measurements of treated films (180 × 180 × 2 mm) revealed an *EAB* of 7.52 GHz and a RL_{min} of − 53.04 dB, consistent with simulation results (Figs. 5g, h and S37). Apart from excellent EMW absorption, practical applications in marine environments also require mechanical robustness, flexibility, and thermal insulation. NC-Fe_{AC2} films retained structural integrity under bending, knotting, and twisting, exhibiting excellent flexibility and mechanical stability (Fig. 5i). Moreover, NC-Fe_{AC2} films demonstrated remarkable ductility and elasticity, tolerating elongation up to 180%. A single 300 mg film could support a 1000 g load, underscoring the exceptional mechanical performance. To further evaluate the influence of mechanical deformation on the EMW absorption performance of the films, we compared its absorption behavior before and after tensile stretching. The results demonstrate that mechanical deformation exerts a negligible effect

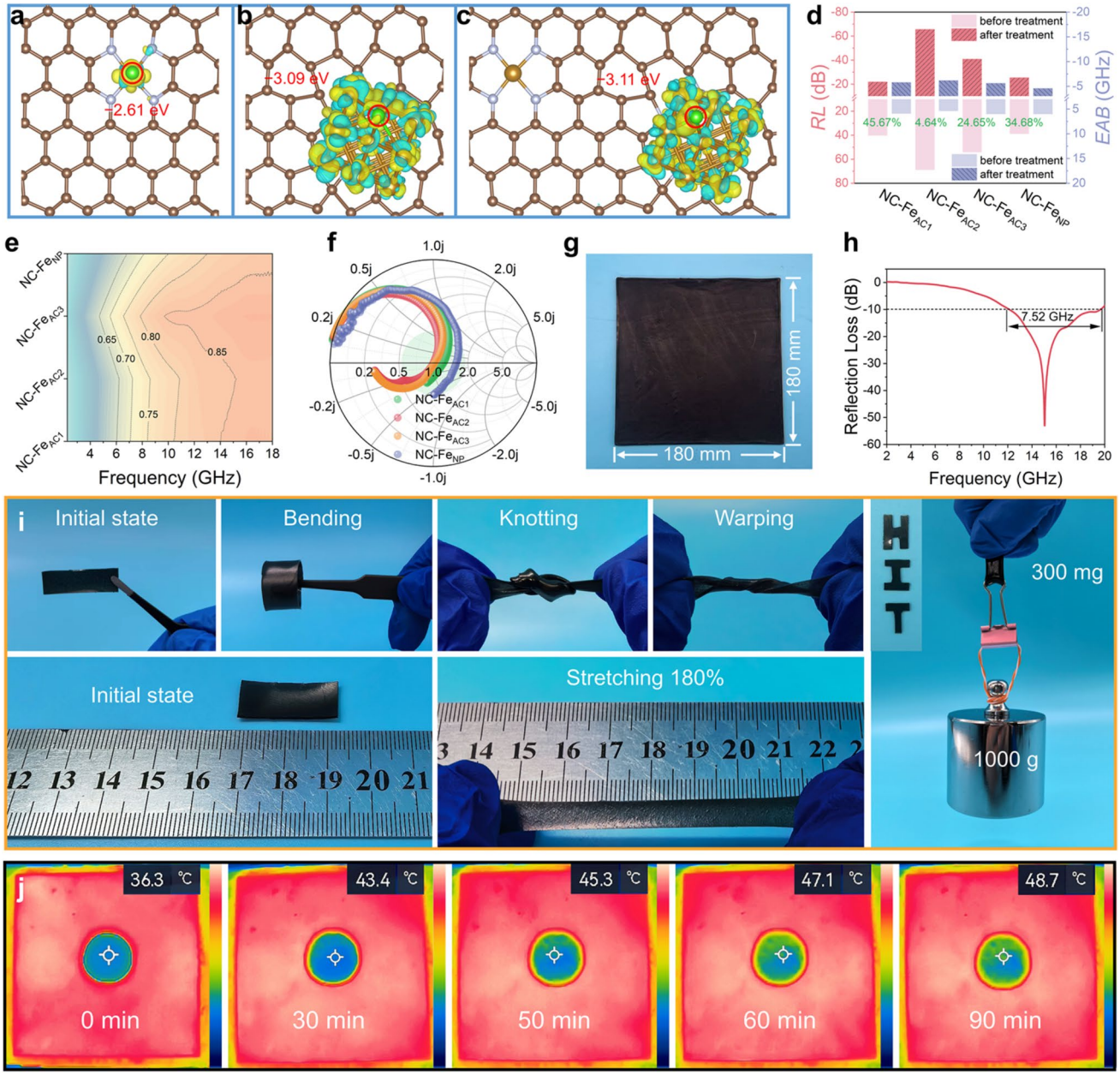

Fig. 5 Difference charge density and Cl^- adsorption energy of **a** Fe_{SA}, **b** Fe_{AC}, and **c** Fe_{SA-AC}. **d** Comparison of *RL* and *EAB* values of NC-Fe_{ACX}, and NC-Fe_{NP} before and after NaCl treatment (single measurement). **e** Contribution of polarization loss to dielectric loss, and **f** smith chart of NC-Fe_{ACX}, and NC-Fe_{NP}. **g** Image of NC-Fe_{AC2} film. **h** EMW performance of NC-Fe_{AC2} film measured by bow-method. **i** Images demonstrate the flexibility and stability of NC-Fe_{AC2} film. **j** Infrared images of NC-Fe_{AC2} film at 100 °C for 0–90 min

on the EMW absorption performance (Fig. S38). Thermal insulation performance was further evaluated for a 2 mm-thick NC-Fe_{AC2} aerogel film (Fig. 5j), which exhibits a low thermal conductivity of 0.077 W M^{-1} k^{-1}. The infrared thermal imaging results showed that, when placed on a 100 °C heating plate for 90 min, the surface temperature increased by only 12.4 °C (Fig. S39), indicating excellent thermal insulation capability. Overall, NC-Fe_{AC2} films integrate efficient EMW absorption (Fig. S40), remarkable mechanical stability, and excellent thermal insulation performance, underscoring the potential for applications in naval vessels

https://doi.org/10.1007/s40820-026-02210-y

and marine equipment, including radar stealth and device protection [50–55].

4 Conclusions

In summary, we developed a Fe cluster–single-atom synergistic absorber (NC-Fe_{AC2}) for high-efficiency electromagnetic wave attenuation under marine environments. At a low loading of 6 wt%, NC-Fe_{AC2} delivers a minimum reflection loss of − 68.78 dB and an effective absorption bandwidth of ~ 6 GHz. Fe clusters (Fe_{AC}) and Fe single atoms (Fe_{SA}) anchored on a π-conjugated carbon support create long-range charge delocalization and multicenter coupling, which strengthen conduction loss. Concurrently, size-tunable Fe_{AC} subtly disrupts the local symmetry of Fe-N_4 coordination sites, inducing reconfiguration of Fe *3d*-N *p* orbital hybridization and asymmetric electron density distribution near the Fermi level. Not only enhances dipole polarization relaxation efficiency, but also optimizes impedance matching via dielectric constant regulation. Thermodynamically, preferred Cl^- adsorption on Fe_{AC} creates locally negative regions that electrostatically shield and stabilize Fe_{SA} sites, suppressing chloride-induced poisoning and preserving dielectric response in marine environments. The NC-Fe_{AC2} film also exhibits straightforward processability, mechanical flexibility, and thermal insulation, highlighting its practicality for multifunctional maritime EM protection and illustrating a generalizable strategy that couples clusters with single atoms to co-optimize performance and durability.

Acknowledgements This work was supported by the financial support from the Defense Industrial Technology Development Program (JCKY2023603C016).

Author Contributions S.Z. contributed to writing—original draft, data curation, methodology, and investigation. X. W. was involved in data curation. R. Z. contributed to data curation. C. L. was involved in data curation. P.Z. contributed to investigation, supervision, funding acquisition, and writing—review and editing. X.Z. was involved in data curation. Z.Z. contributed to data curation. Y.L. was involved in data curation. C.C. contributed to data curation. Y.Y. was involved in writing—review and editing, and supervision. L.X. contributed to conceptualization, supervision, funding acquisition, and writing—review and editing.

Declarations

Conflict of interest The authors declare no interest conflict. They have no known competing financial interests or personal relationships that could have appeared to influence the work reported in this paper.

Supplementary Information The online version contains supplementary material available at https://doi.org/10.1007/s40820-026-02210-y.

References

1. J. Tao, J. Zhou, Z. Yao, J. Wang, L. Xu et al., Multi-field coupled motion induces electromagnetic wave absorbing property regeneration of elastomer in marine environment. Adv. Funct. Mater. **34**(12), 2310640 (2024). https://doi.org/10.1002/adfm.202310640
2. X. Zeng, X. Deng, Z. Yu, X. Zhang, J. Lu et al., Evolution of Fe single atom in SiOC ceramic fibers and their high-temperature and ultrathin electromagnetic wave absorption. Adv. Mater. **38**(14), e21533 (2026). https://doi.org/10.1002/adma.202521533
3. L. Zhou, P. Hu, M. Bai, N. Leng, B. Cai et al., Harnessing the electronic spin states of single atoms for precise electromagnetic modulation. Adv. Mater. **37**(7), 2418321 (2025). https://doi.org/10.1002/adma.202418321
4. X. Kang, F. Yang, Z. Zhang, H. Liu, S. Ge et al., A corrosion-resistant RuMoNi catalyst for efficient and long-lasting seawater oxidation and anion exchange membrane electrolyzer. Nat. Commun. **14**, 3607 (2023). https://doi.org/10.1038/s41467-023-39386-5
5. H. Ren, T. Li, H. Wang, Z. Guo, T. Chen et al., Two birds with one stone: superhelical chiral polypyrrole towards high-performance electromagnetic wave absorption and corrosion protection. Chem. Eng. J. **427**, 131582 (2022). https://doi.org/10.1016/j.cej.2021.131582
6. X.-F. Yang, A. Wang, B. Qiao, J. Li, J. Liu et al., Single-atom catalysts: a new frontier in heterogeneous catalysis. Acc. Chem. Res. **46**(8), 1740–1748 (2013). https://doi.org/10.1021/ar300361m

7. X.-C. Zhang, M. Zhang, M.-Q. Wang, L. Chang, L. Li et al., Metal single-atoms toward electromagnetic wave-absorbing materials: insights and perspective. Adv. Funct. Mater. **34**(44), 2405972 (2024). https://doi.org/10.1002/adfm.202405972
8. W.-H. Li, J. Yang, D. Wang, Long-range interactions in diatomic catalysts boosting electrocatalysis. Angew. Chem. Int. Ed. **61**(52), e202213318 (2022). https://doi.org/10.1002/anie.202213318
9. X. Zhang, Y. Shi, J. Xu, Q. Ouyang, X. Zhang et al., Identification of the intrinsic dielectric properties of metal single atoms for electromagnetic wave absorption. Nano-Micro Lett. **14**(1), 27 (2021). https://doi.org/10.1007/s40820-021-00773-6
10. J. Xu, B. Li, Z. Ma, X. Zhang, C. Zhu et al., Multifunctional film assembled from N-doped carbon nanofiber with co–N_4–O single atoms for highly efficient electromagnetic energy attenuation. Nano-Micro Lett. **16**(1), 240 (2024). https://doi.org/10.1007/s40820-024-01440-2
11. H. Xu, M. Liu, L. Huang, X. Zhang, Z. Ma et al., Enhanced dielectric loss *via* six-coordinated Er single atoms on porous carbon nanofibers for high-performance electromagnetic wave absorption. Adv. Funct. Mater. **35**(32), 2502952 (2025). https://doi.org/10.1002/adfm.202502952
12. Y. Shi, Z. Ma, X. Zhang, F. Yan, Y. Zhao et al., Flexible film constructed by asymmetrically-coordinated $La_1N_4Cl_1$ moieties on interconnected nitrogen-doped graphene nanocages for high-efficiency electromagnetic wave absorption. Adv. Funct. Mater. **34**(16), 2313483 (2024). https://doi.org/10.1002/adfm.202313483
13. X. Zhang, X. Zhu, S. Bo, C. Chen, M. Qiu et al., Identifying and tailoring C–N coupling site for efficient urea synthesis over diatomic Fe–Ni catalyst. Nat. Commun. **13**, 5337 (2022). https://doi.org/10.1038/s41467-022-33066-6
14. S. Zhang, J. Wu, M. Zheng, X. Jin, Z. Shen et al., Fe/Cu diatomic catalysts for electrochemical nitrate reduction to ammonia. Nat. Commun. **14**, 3634 (2023). https://doi.org/10.1038/s41467-023-39366-9
15. N. Xu, Y. Jin, Q. Liu, M. Yu, X. Wang et al., Rational design of diatomic active sites for elucidating oxygen evolution reaction performance trends. Angew. Chem. Int. Ed. **64**, e202413749 (2025). https://doi.org/10.1002/anie.202413749
16. Y. Zhan, Z.-B. Ding, F. He, X. Lv, W.-F. Wu et al., Active site switching of Fe-N-C as a chloride-poisoning resistant catalyst for efficient oxygen reduction in seawater-based electrolyte. Chem. Eng. J. **443**, 136456 (2022). https://doi.org/10.1016/j.cej.2022.136456
17. J. Qin, H. Liu, P. Zou, R. Zhang, C. Wang et al., Altering ligand fields in single-atom sites through second-shell anion modulation boosts the oxygen reduction reaction. J. Am. Chem. Soc. **144**(5), 2197–2207 (2022). https://doi.org/10.1021/jacs.1c11331
18. G. Li, J. Liu, C. Xu, H. Chen, H. Hu et al., Regulating the Fe-spin state by Fe/Fe3C neighbored single Fe-N4 sites in defective carbon promotes the oxygen reduction activity. Energy Storage Mater. **56**, 394–402 (2023). https://doi.org/10.1016/j.ensm.2023.01.030
19. Q. Ban, Y. Song, L. Li, H. Zhang, X. Wu et al., Confined diffusion engineering of FeCoNi-embedded hollow carbon microcage toward controllable electromagnetic wave absorption and anticorrosive polyvinylidene fluoride composite in marine environment. Small **21**(41), e08008 (2025). https://doi.org/10.1002/smll.202508008
20. L. Duan, J. Zhou, J. Tao, Y. Liu, Y. Yan et al., Genome engineering of materials based on Ce doping, high-performance electromagnetic wave absorber for marine environment. Compos. Part B Eng. **287**, 111882 (2024). https://doi.org/10.1016/j.compositesb.2024.111882
21. X. Zhang, X. Zhang, H. Yuan, K. Li, Q. Ouyang et al., CoNi nanoparticles encapsulated by nitrogen-doped carbon nanotube arrays on reduced graphene oxide sheets for electromagnetic wave absorption. Chem. Eng. J. **383**, 123208 (2020). https://doi.org/10.1016/j.cej.2019.123208
22. H. Zhai, L. Wu, L. Yu, L. Li, G. Wan et al., Polypyrrole/NiFe-layered double hydroxide composite as an anticorrosive microwave absorber. J. Mater. Chem. C. **12**(29), 11001–11011 (2024). https://doi.org/10.1039/d4tc01485e
23. T. Zhao, Z. Jia, J. Liu, Y. Zhang, G. Wu et al., Multiphase interfacial regulation based on hierarchical porous molybdenum selenide to build anticorrosive and multiband tailorable absorbers. Nano-Micro Lett. **16**(1), 6 (2023). https://doi.org/10.1007/s40820-023-01212-4
24. P. Liu, Z. He, X. Li, L. Ding, S. Liu et al., Multifunctional hollow carbon microspheres enable superior electromagnetic wave response and corrosion barrier. Adv. Mater. **37**(35), 2500646 (2025). https://doi.org/10.1002/adma.202500646
25. H. Liu, W. Xu, H. Ren, D. Li, J. He et al., Integrated comprehensive protection coating achieved by ligand engineering modulated MXene@LDH heterojunction with anti-corrosion, electromagnetic wave absorption and fire safety. Chem. Eng. J. **486**, 150444 (2024). https://doi.org/10.1016/j.cej.2024.150444
26. J. Yao, J. Zhou, L. Lu, F. Yang, Z. Yao et al., Rare earth lanthanum pinning effect for corrosion resistance ultraefficient microwave absorption FeCo@rGO composites. J. Mater. Sci. Technol. **177**, 181–190 (2024). https://doi.org/10.1016/j.jmst.2023.07.075
27. J. Song, X. Zhao, S. Yuan, H. Zheng, Z. Jin et al., Engineering synergistic coatings: high-performance Cu/Co bimetal-modified fibrous carbon networks for enhanced anticorrosion and electromagnetic wave absorption in harsh environments. Prog. Org. Coat. **208**, 109426 (2025). https://doi.org/10.1016/j.porgcoat.2025.109426
28. J. Lu, Q. Lu, Y. Guo, X. Chen, Z. Yin et al., Cobalt atom-cluster interactions synergistically enhance the activity of oxygen reduction reaction in seawater. Energy Storage Mater. **65**, 103093 (2024). https://doi.org/10.1016/j.ensm.2023.103093
29. M. Zhang, H. Li, J. Chen, F.-X. Ma, L. Zhen et al., High-loading Co single atoms and clusters active sites toward enhanced electrocatalysis of oxygen reduction reaction for high-performance Zn–air battery. Adv. Funct. Mater. **33**(4), 2209726 (2023). https://doi.org/10.1002/adfm.202209726
30. P. Rao, Y. Liu, X. Shi, Y. Yu, Y. Zhou et al., Protection of Fe single-atoms by Fe clusters for chlorine-resistant oxygen

 https://doi.org/10.1007/s40820-026-02210-y

reduction reaction. Adv. Funct. Mater. **34**(46), 2407121 (2024). https://doi.org/10.1002/adfm.202407121

31. S. Tian, Q. Fu, W. Chen, Q. Feng, Z. Chen et al., Carbon nitride supported Fe_2 cluster catalysts with superior performance for alkene epoxidation. Nat. Commun. **9**, 2353 (2018). https://doi.org/10.1038/s41467-018-04845-x
32. F.-Y. Zheng, R. Li, S. Xi, F. Ai, J. Wang, Engineering an iron atom-cluster nanostructure towards efficient and durable electrocatalysis. J. Mater. Chem. A **11**(15), 8202–8212 (2023). https://doi.org/10.1039/d3ta00232b
33. X. Wan, Q. Liu, J. Liu, S. Liu, X. Liu et al., Iron atom–cluster interactions increase activity and improve durability in Fe–N–C fuel cells. Nat. Commun. **13**, 2963 (2022). https://doi.org/10.1038/s41467-022-30702-z
34. C. Liu, R. Yang, J. Wang, B. Liu, X. Chang et al., Synergistic catalysts with Fe single atoms and Fe_3C clusters for accelerated oxygen adsorption kinetics in oxygen reduction reaction. Angew. Chem. Int. Ed. **64**(21), e202501266 (2025). https://doi.org/10.1002/anie.202501266
35. B. Qu, C. Zhu, C. Li, X. Zhang, Y. Chen, Coupling hollow Fe_3O_4–Fe nanoparticles with graphene sheets for high-performance electromagnetic wave absorbing material. ACS Appl. Mater. Interfaces **8**(6), 3730–3735 (2016). https://doi.org/10.1021/acsami.5b12789
36. J. Zou, C. Chen, Y. Chen, Y. Zhu, Q. Cheng et al., Facile steam-etching approach to increase the active site density of an ordered porous Fe–N–C catalyst to boost oxygen reduction reaction. ACS Catal. **12**(8), 4517–4525 (2022). https://doi.org/10.1021/acscatal.2c00408
37. K. Zhang, Y. Yan, Z. Wang, G. Ma, D. Jia et al., Integration of electrical properties and polarization loss modulation on atomic Fe–N-RGO for boosting electromagnetic wave absorption. Nano-Micro Lett. **17**(1), 46 (2024). https://doi.org/10.1007/s40820-024-01518-x
38. D. Cao, H. Xu, H. Li, C. Feng, J. Zeng et al., Volcano-type relationship between oxidation states and catalytic activity of single-atom catalysts towards hydrogen evolution. Nat. Commun. **13**, 5843 (2022). https://doi.org/10.1038/s41467-022-33589-y
39. A. Kormányos, E. Kecsenovity, A. Honarfar, T. Pullerits, C. Janáky, Hybrid FeNiOOH/α-Fe_2O_3/graphene photoelectrodes with advanced water oxidation performance. Adv. Funct. Mater. **30**(31), 2002124 (2020). https://doi.org/10.1002/adfm.202002124
40. A.M. Jubb, H.C. Allen, Vibrational spectroscopic characterization of hematite, maghemite, and magnetite thin films produced by vapor deposition. ACS Appl. Mater. Interfaces **2**(10), 2804–2812 (2010). https://doi.org/10.1021/am1004943
41. D.L.A. de Faria, S. Venâncio Silva, M.T. de Oliveira, Raman microspectroscopy of some iron oxides and oxyhydroxides. J. Raman Spectrosc. **28**(11), 873–878 (1997)
42. J. Wang, R. You, C. Zhao, W. Zhang, W. Liu et al., N-coordinated dual-metal single-site catalyst for low-temperature CO oxidation. ACS Catal. **10**(4), 2754–2761 (2020). https://doi.org/10.1021/acscatal.0c00097
43. Q. Jia, N. Ramaswamy, H. Hafiz, U. Tylus, K. Strickland et al., Experimental observation of redox-induced Fe–N switching behavior as a determinant role for oxygen reduction activity. ACS Nano **9**(12), 12496–12505 (2015). https://doi.org/10.1021/acsnano.5b05984
44. Y. Xie, X. Chen, K. Sun, J. Zhang, W.-H. Lai et al., Direct oxygen-oxygen cleavage through optimizing interatomic distances in dual single-atom electrocatalysts for efficient oxygen reduction reaction. Angew. Chem. Int. Ed. **62**(17), e202301833 (2023). https://doi.org/10.1002/anie.202301833
45. Q. Tang, Q. Hao, Q. Zhu, J. Wu, K. Huang et al., Intrinsic electron transfer in heteronuclear dual-atom sites facilitates selective electrocatalytic carbon dioxide reduction. Adv. Energy Mater. **15**(7), 2403778 (2025). https://doi.org/10.1002/aenm.202403778
46. L. Wu, Y. Chen, C. Shao, L. Wang, B. Li, Engineering synergetic Fe-co atomic pairs anchored on porous carbon for enhanced oxygen reduction reaction. Adv. Funct. Mater. **34**(48), 2408257 (2024). https://doi.org/10.1002/adfm.202408257
47. X. Liu, J. Zhou, Y. Xue, X. Lu, Structural engineering of hierarchical magnetic/carbon nanocomposites *via in situ* growth for high-efficient electromagnetic wave absorption. Nano-Micro Lett. **16**(1), 174 (2024). https://doi.org/10.1007/s40820-024-01396-3
48. W. You, H. Bi, W. She, Y. Zhang, R. Che, Dipolar-distribution cavity γ-Fe_2O_3@C@α-MnO_2 nanospindle with broadened microwave absorption bandwidth by chemically etching. Small **13**(5), 1602779 (2017). https://doi.org/10.1002/smll.201602779
49. X.-X. Fan, M. Zhang, X.-C. Zhang, L. Li, M.-S. Cao, A pomegranate-like nanolayer featuring a core-shell architectural design for thermal-mechanical-electromagnetic responses and sensor. Adv. Funct. Mater. **35**(16), 2421144 (2025). https://doi.org/10.1002/adfm.202421144
50. R. Hu, J. Luo, H. Wen, C. Liu, J. Peng et al., Enhanced electromagnetic energy conversion in an entropy-driven dual-magnetic system for superior electromagnetic wave absorption. Adv. Funct. Mater. **35**(14), 2418304 (2025). https://doi.org/10.1002/adfm.202418304
51. B. Yao, X. Xu, H. Li, Z. Han, J. Hao et al., Soft liquid-metal/elastomer foam with compression-adjustable thermal conductivity and electromagnetic interference shielding. Chem. Eng. J. **410**, 128288 (2021). https://doi.org/10.1016/j.cej.2020.128288
52. B. Yao, X. Xu, Z. Han, W. Xu, G. Yang et al., Cephalopod-inspired polymer composites with mechanically tunable infrared properties. Sci. Bull. **68**(23), 2962–2972 (2023). https://doi.org/10.1016/j.scib.2023.10.039
53. J. Wang, W. Ming, L. Chen, T. Song, M. Yele et al., MoS_2 lubricate-toughened MXene/ANF composites for multifunctional electromagnetic interference shielding. Nano-Micro Lett. **17**(1), 36 (2024). https://doi.org/10.1007/s40820-024-01496-0
54. S. Wang, Y. Li, D. Lei, M. Ma, X. He, Butterfly wing-inspired carbon fiber with confined growth of wave-trapping

architecture for broadband electromagnetic wave absorption. Adv. Funct. Mater. (2025). https://doi.org/10.1002/adfm.202526212

55. X. Zeng, L. Wu, X. Yang, Z. Wu, X. Xu et al., Design of gel-based materials for electromagnetic wave absorption. Adv. Funct. Mater. **35**(33), 2502671 (2025). https://doi.org/10.1002/adfm.202502671

 https://doi.org/10.1007/s40820-026-02210-y